PNAS RESEARCH ARTICLE | PHYSICS

Anomalous phase separation in a correlated electron system: Machine-learning–enabled large-scale kinetic Monte Carlo simulations

Sheng Zhang[a], Puhan Zhang[a], and Gia-Wei Chern[a,1]

Edited by Elbio Dagotto, The University of Tennessee College of Arts and Sciences, Knoxville, TN; received November 8, 2021; accepted March 25, 2022 by Editorial Board Member Mehran Kardar

Phase separation plays a central role in the emergence of unusual functionalities of correlated electron materials. The structure of the mixed-phase states depends strongly on the nonequilibrium phase-separation dynamics, which have so far yet to be systematically investigated, especially on the theoretical side. With the aid of modern machine-learning methods, we demonstrate large-scale kinetic Monte Carlo simulations of the phase-ordering process for the Falicov–Kimball model, which is one of the canonical strongly correlated electron systems. We uncover unusual relaxation dynamics with domain growth occurring simultaneously at two different length scales. At a smaller scale, the phase-separation instability leads to the growth of insulating checkerboard clusters in a metallic background. Interestingly, a hidden dynamical breaking of the sublattice symmetry gives rise to the emergence and coarsening of superclusters, which are aggregates of the checkerboard clusters whose f electrons reside on the same sublattice, at a larger scale. Arrested growth of the checkerboard patterns and of the superclusters is shown to result from a correlation-induced self-trapping mechanism. Glassy behaviors similar to the one reported in this work could be generic for other correlated electron systems.

strongly correlated electron | phase separation | machine learning

Complex mesoscopic textures are ubiquitous in strongly correlated electron materials (1–9). Notable examples include stripe and checkerboard patterns in high-T_c superconductors and nanoscale mixture of metallic and insulating domains in manganites. Not only are these mesoscopic textures of fundamental importance in correlated electron physics; they are also central to the emergence of unusual functionalities in these materials. The nanoscale patterns in correlated electron materials often result from phase-separation instability driven by the electron correlation effects. Indeed, a generic feature of lightly doped Mott insulators is the strong tendency toward phase separation in which the doped holes are expelled from the locally insulating antiferromagnetic domains (10–15). Although considerable efforts have been devoted to understanding the phase separation mechanisms and properties of the mixed-phase states in strongly correlated electron materials, the nonequilibrium pattern-formation dynamics in such systems are poorly understood.

On the other hand, intermediate states with complex structures have been observed in discontinuous phase transitions of many classical systems (16, 17), ranging from binary alloys and glasses to polymer blends and active matters. The kinetics of first-order transition are a mature subject with a long history (18–20). In such studies, one is concerned with the evolution of a system from an unstable or metastable state toward its preferred equilibrium phase, a process that is often characterized by the appearance of complex spatial–temporal patterns. Several numerical techniques, including kinetic Monte Carlo, molecular dynamics simulations, and phase-field modeling, have been developed for large-scale simulations of phase-separation phenomena (21–23). Of particular interest in such studies is the dynamical universality class and the associated universal growth law (24, 25). The phase-ordering process is usually modeled by dynamical equations for the order-parameter fields that describe the structure of the symmetry-breaking state. However, most of the works in this field are based on empirical energy models that often cannot capture the complex and nonlocal interaction of the order-parameter fields, especially for correlated electron systems.

A comprehensive modeling of correlation-driven phase separation thus needs to take into account the microscopic electronic processes and the mesoscopic pattern formation dynamics simultaneously. For example, one could obtain the driving forces on the order-parameter fields by integrating out the electrons on the fly, which means the electronic structure problem is to be solved at every timestep of the macroscopic dynamics

Significance

Phase separation is crucial to the functionalities of many correlated electron materials with notable examples including colossal magnetoresistance in manganites and high-T_c superconductivity in cuprates. However, the nonequilibrium phase-separation dynamics in such systems are poorly understood theoretically, partly because the required multiscale modeling is computationally very demanding. With the aid of machine-learning methods, we have achieved large-scale dynamical simulations in a representative correlated electron system. We observe an unusual relaxation process that is beyond the framework of classical phase-ordering theories. We also uncover a correlation-induced freezing behavior, which could be a generic feature of phase separation in correlated electron systems.

Author affiliations: [a]Department of Physics, University of Virginia, Charlottesville, VA 22904

Author contributions: G.-W.C. designed research; S.Z., P.Z., and G.-W.C. performed research; S.Z. and G.-W.C. analyzed data; and S.Z., P.Z., and G.-W.C. wrote the paper.

The authors declare no competing interest.

This article is a PNAS Direct Submission. E.D. is a guest editor invited by the Editorial Board.

[1]To whom correspondence may be addressed. Email: gchern@virginia.edu

This article contains supporting information online at https://www.pnas.org/lookup/suppl/doi:10.1073/pnas.2119957119/-/DCSupplemental.

Published April 29, 2022.

simulation. However, the repeated solution of the electronic problem, obtained using techniques ranging from exact diagonalization to more sophisticated many-body methods, can be prohibitively expensive for large-scale simulations. Such computational obstacles for multiscale simulations are partly the reason for the lack of progress in our understanding of the phase-ordering dynamics in correlated electron materials.

In this paper we make an important step toward the goal of multiscale dynamical modeling of strongly correlated electron systems by utilizing the machine-learning techniques to develop an efficient yet accurate energy model. We demonstrate a large-scale simulation of phase separation phenomena in the Falicov–Kimball (FK) model (26), which is one of the canonical correlated electron systems. Originally put forward as a limiting case of the Hubbard model (27), the FK model was later independently proposed to describe semiconductor–metal transitions in rare-earth and transition-metal compounds (26). The FK model describes conducting c electrons interacting with localized f electrons through an on-site repulsive interaction. Its relative simplicity allows for numerically exact solutions, which serve as important benchmarks for sophisticated many-body methods (28). The FK model itself has rich phase diagrams and is one of the best-studied correlated electron systems that exhibit complex pattern formation and phase separation (29–38). In particular, the FK model offers the proof of principle that stripe and checkerboard orders, which play a prominent role in the high-T_c superconductivity phenomenology, can arise from a pure electronic correlation effect (30–33), such as the Kivelson–Emery scenario of phase separation.

We consider the spinless FK Hamiltonian on a square lattice (28, 33) in this work:

$$\mathcal{H} = -t_{\rm nn} \sum_{\langle ij \rangle} c_i^\dagger c_j + U \sum_i c_i^\dagger c_i \, n_i^f . \qquad [1]$$

Here $c_i^\dagger$ (c_i) is the creation (annihilation) operator for a c electron at site i; $\langle ij \rangle$ denotes nearest-neighbor pairs on the lattice; n_i^f is the occupation number of the f electron; $t_{\rm nn}$ is the nearest-neighbor hopping constant, which also serves as the energy unit; and $U > 0$ is the strength of on-site repulsive interaction. Due to the quadratic nature of the c-electron Hamiltonian, equilibrium phases of the FK model can in principle be exactly solved numerically by combining the classical Monte Carlo method for f electrons with exact diagonalization (ED) for c electrons (36–38). Moreover, within the framework of the dynamical mean-field theory, the quantum impurity problem associated with the FK model can also be exactly solved (28, 35).

The equilibrium phases of the square-lattice FK model have been extensively studied over the years. Exactly at half-filling for both c and f electrons, the ground state exhibits a charge density wave (CDW) order with the f electrons forming a checkerboard pattern (37, 38). Away from half-filling, the model shows various stripe and incommensurate phases (32, 33). With slight electron or hole doping, a phase-separated regime is stabilized (33, 35, 36), a scenario similar to that of the Hubbard model. Despite being one of the prominent models for electronic phase separation, the phase-ordering dynamics in FK systems have never been studied. Important questions, such as whether the system exhibits dynamical scaling and what is the domain-growth law, remain open.

To address these issues, we formulate a kinetic Monte Carlo (kMC) method (23, 39) to simulate the phase-ordering process of the FK model subject to a temperature quench. While the c electrons have well-defined dynamics in the FK Hamiltonian, the f electrons in the FK model, with $n_i^f = 0$ or 1, are static discrete variables, similar to classical Ising spins. To endow the f electron with dynamics, a random-walk algorithm is used to model their diffusive motion. At every timestep, an attempt is made to move a randomly chosen f electron to one of its empty neighbors. Whether the update is accepted is determined by the standard Metropolis criterion (23). We further assume that the equilibration of c electrons is much faster compared with the random walks of f electrons, analogous to the Born–Oppenheimer approximation in quantum molecular dynamics (40). Consequently, the motion of the heavier f electrons depends on the free energy of the quasi-equilibrium c electrons before and after the update. The acceptance probability of such a nearest-neighbor move is

$$p_{i\to j} = \frac{1}{4} \min\left(1, e^{-\Delta E_{i\to j}/k_B T}\right), \qquad [2]$$

where $\Delta E_{i\to j}$ is the free-energy difference of c electrons due to the hopping of the f electron from site i to j. The probability that the f electron stays put is $p_{i\to i} = 1 - \sum_j p_{i\to j}$. We note in passing that lattice gas systems combined with kMC simulations are widely used to describe phase separation phenomena in conventional alloys (41, 42). However, most works are based on empirical energy models, often formulated as effective classical Ising Hamiltonians. As we demonstrate below, deep neural networks, trained from exact solutions, can be used to obtain an accurate and efficient energy model for the f electrons of the FK system.

The c-electron free energy can be computed using either ED or more efficient techniques such as the kernel polynomial method (43). However, the quantum kMC simulation described above is very time consuming for large systems, since one needs to solve the electron tight-binding problem multiple times to update just one f electron. To overcome this computational bottleneck, we apply the machine-learning (ML) methods that have been exploited to improve the efficiency of quantum molecular dynamics simulations (44–48). Similar approaches have also been used to enable large-scale quantum spin dynamics in double-exchange systems (49, 50). The central idea of our approach, summarized in Fig. 1*A*, is based on the principle of locality (51, 52) or what Walter Kohn termed the nearsightedness of electronic matter. In our case, the locality principle indicates that the energy change $\Delta E_{i\to j}$ depends only on f-electron configuration in the neighborhood of the local update. Specifically, the energy change $\Delta E_{i\to j}$ of a local update is assumed to depend on neighborhood configuration through universal functions

$$\Delta E_{i\to j} = \varepsilon(\hat{\mathbf{n}}_{ij}, \mathcal{C}_i), \qquad [3]$$

where $\hat{\mathbf{n}}_{ij} = \pm\hat{\mathbf{x}}, \pm\hat{\mathbf{y}}$ denotes the orientation of the $i \to j$ bond, and $\mathcal{C}_i = \left\{ n_k^f \,\middle|\, |\mathbf{r}_k - \mathbf{r}_i| \le r_c \right\}$ describes the neighborhood f-electron configuration up to a cutoff radius r_c. The complex dependence of the energy function $\varepsilon(\cdot)$ on the local environment is then encoded in a neural network to be trained by exact solutions from small systems.

Importantly, the effective energy function $\varepsilon(\cdot)$ is required to preserve the site symmetry of the lattice. This can be achieved by a proper representation, also known as a descriptor, of the neighborhood configuration $\mathcal{C}_i$. To this end, we first note that the distribution $\{n_j^f\}$ of f electrons in the neighborhood corresponds to a reducible representation of the point group associated with site i. By decomposing it into the irreducible representations (IRs), the neighborhood configuration $\mathcal{C}_i$ is translated into the amplitudes of the IRs. Effective coordinates $\{G_\ell\}$ that are invariant under the symmetry operations of the on-site point group are

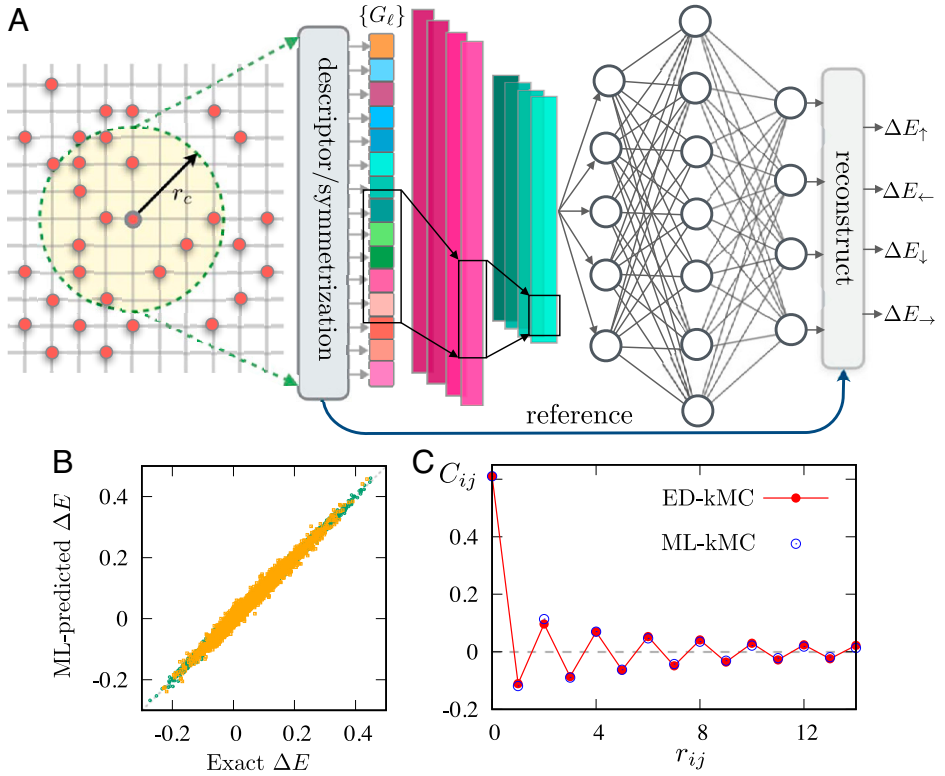

Fig. 1. (*A*) Schematic diagram of NN energy model for kMC dynamics simulation of the FK system. A descriptor is used to construct effective coordinates $\{G_\ell\}$ from neighborhood f-electron configuration $\{n_j^f\}$ up to a cutoff $r_c = 10$. These feature variables $\{G_\ell\}$ are input to the NN that predicts the energy differences ΔE at the output. (*B*) ML-predicted ΔE versus exact values. The circles and squares denote training and test datasets, respectively. (*C*) Comparison of f-electron correlation function $C_{ij} = \langle n_i^f n_j^f \rangle$ obtained from ED- and ML-kMC simulations on a 30 × 30 lattice after 5,000 steps from the same initial condition.

obtained from the bispectrum coefficients of the IRs (53). Details of this construction can be found in *SI Appendix*, section S1.

The generalized coordinates $\{G_\ell\}$, also known as feature variables, are then fed into a neural network (NN). Due to the discrete binary nature of f-electron occupation number, a convolutional NN is used to enhance recognition of the major features in the input. The output from the convolutional layers then propagates to a fully connected feedforward NN, which in turn produces the predicted energy differences $\Delta E_{i\to j}$. We have built an eight-layer NN model trained by dataset obtained from ED-kMC simulations on a 30 ×30 lattice; see *SI Appendix* for details of the neural network structure, dataset selection, and training process. As shown in Fig. 1*B*, the ML-predicted energy difference $\Delta E_{i\to j}$ agrees well with the exact values. We further show that the f-electron correlation function $C_{ij} = \langle n_i^f n_j^f \rangle$ obtained from kMC simulations based on the NN model also agrees well with that of exact kMC simulations (Fig. 1*C*).

With the properly benchmarked NN energy model, we perform large-scale ML-kMC simulations on the FK model with up to 10^5 lattice sites. Our goal is to study the growth dynamics of checkerboard clusters after a temperature quench. To this end, we consider slightly doped c electrons with a filling fraction $\rho_c = 0.55$ and a low f-electron density of $\rho_f = 0.187$. The repulsive interaction is set at $U = 2\,t_{\rm nn}$. The low-temperature phase corresponding to these parameters is a phase-separated mixture of insulating CDW clusters, corresponding to checkerboard ordering of f electrons and metallic domains in the absence of f electrons (35). Some stripe orders have also been observed. In our simulations, the system is initially prepared in a state with random distribution of f electrons, and the temperature is suddenly reduced to $T = 0.05\,t_{\rm nn}$ at time $t = 0$. Fig. 2 *A*–*C* shows snapshots of the f-electron configuration at different simulation times after the quench. The green shades highlight individual CDW clusters. A close-up view of the phase-separated phase, shown in Fig. 2*D*, clearly displays several checkerboard clusters and some diagonal stripes of the f electrons.

Fig. 2*E* shows the probability distribution functions $P(s)$ of the CDW clusters at different times after quench. Here the cluster size s is defined as the number of f electrons in a CDW cluster, and $s = 1$ corresponds to an isolated f electron. The distribution functions seem to be well approximated by an exponential tail $P(s) \sim \exp(-\text{const} \times s)$ at large s, similar to the subcritical regime of a percolation transition. Although the overall probability of finding large-size CDW clusters increases with time, it remains exponentially small for very large CDW clusters. To further characterize the mixed-phase states, Fig. 2*F* shows the histogram of the on-site c-electron occupation number $\langle c_i^\dagger c_i \rangle$ obtained by ED on a smaller 30 × 30 lattice. The sharp peak at $n_c \sim 0.2$ corresponds to lattice sites occupied by an f electron $n_i^f = 1$, while the broad peak at $n_c \sim 0.65$ comes from sites without an f electron. The average c-electron density in the metallic region, which consists entirely of the empty sites, is $n^c_{\rm metal} \approx 0.626$. On the other hand, both peaks in Fig. 2*F* contribute to the c electron in the CDW clusters, with an average density $n^c_{\rm CDW} \approx 0.472$.

Fig. 2*G* shows the increase of average checkerboard cluster size $\langle s \rangle$ with time, indicating the aggregation of f electrons to form CDW order during the phase separation. Since the number of f electrons is conserved, the growth of checkerboard domains is similar to the phase separation of a conserved order parameter that is expected to follow the $t^{1/3}$ power-law growth predicted by the Lifshitz–Slyozov–Wagner (LSW) theory (54, 55) or the model-B dynamics (24, 56). As shown in Fig. 2 *G*, *Inset*, the typical

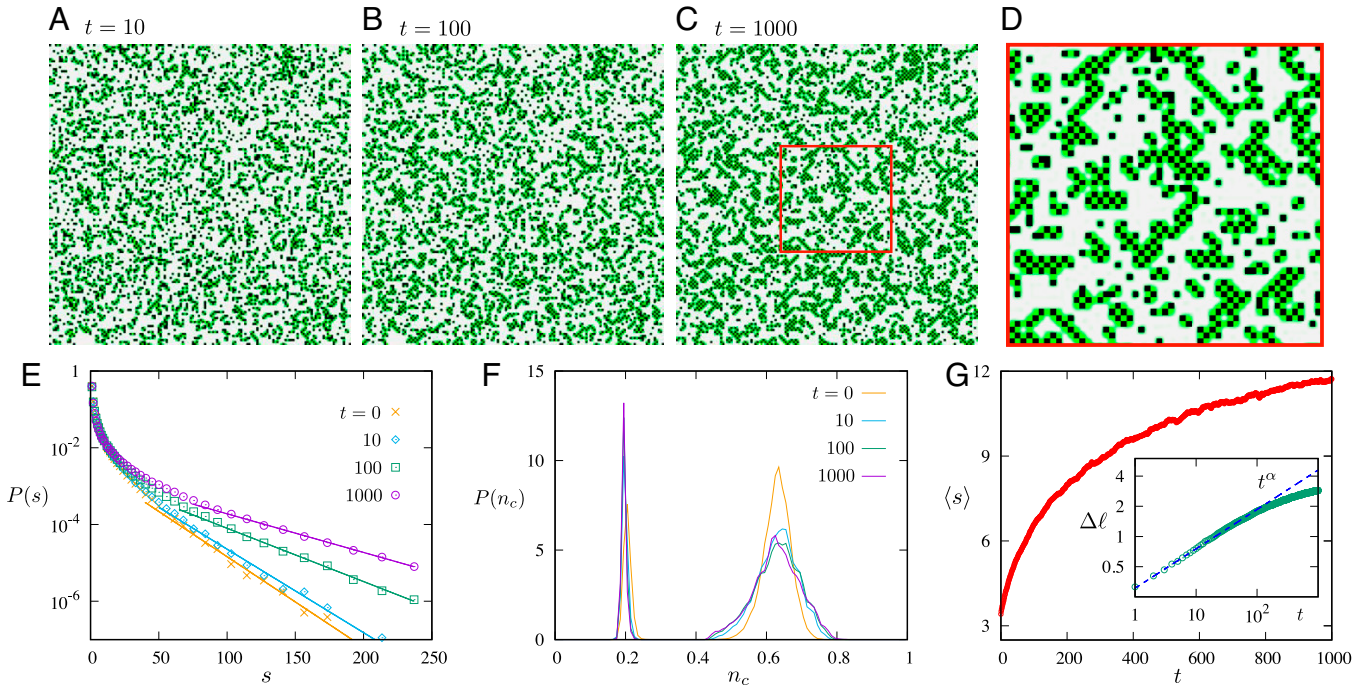

Fig. 2. Summary of the ML-kMC simulations of the CDW-metal phase-separation dynamics. (*A–C*) Snapshots of the *f*-electron configuration $\{n_i^f\}$ and the associated CDW clusters highlighted by green shade obtained from the ML-kMC simulations on a 150 × 150 square-lattice FK model. (*D*) A close-up view of the *f*-electron configuration corresponding to the red square in *C*. Here time *t* is measured in terms of 100 MC steps. (*E*) The probability distribution function $P(s)$ of the CDW cluster size at different simulation times during the phase separation. Here the size *s* is defined as the total number of *f* electrons in a CDW cluster. The straight lines in the semilog plot are exponential fits of the distribution function at large *s*. (*F*) Averaged histogram of the on-site *c*-electron occupation number $\langle c_i^\dagger c_i \rangle$ at different times obtained from ED-kMC on a smaller 30 × 30 lattice. (*G*) Average size $\langle s \rangle$ of checkerboard cluster as a function of time obtained from ML-kMC on a 150 × 150 lattice. *Inset* shows the time dependence of the characteristic length scale $\ell(t) = \ell_0 + \Delta\ell$, where $\ell = \langle s \rangle^{1/2}$. The dashed line indicates a power-law growth with exponent $\alpha \approx 0.35$.

length scale of checkerboard clusters indeed increases according to a power-law $\Delta\ell \sim t^\alpha$, even early in the phase-separation process, although the exponent $\alpha \approx 0.35$ is slightly higher than the LSW prediction. The discrepancy here can be attributed to the fact that the LSW scaling occurs only for coarsening of very large domains at late times (57).

However, this power-law regime lasts only a short duration and the growth slows down significantly at late stage. This stagnation of domain growth cannot be attributed to the finite-size effect since the average cluster size is still significantly smaller than the system sizes at late times. Instead, the freezing of the checkerboard clusters, which is discussed in more detail below, is related to a sublattice symmetry breaking hidden in the phase separation process. To illustrate this effect, we use different colors to label the f electrons at the two sublattices of the square lattice. As shown in Fig. 3 *A–C*, *Top*, while the sizes of checkerboard clusters remain small, f electrons residing on the same sublattice tend to stick together, thus forming superclusters of the checkerboards. Crucially, the formation of such superstructures breaks the Z_2 sublattice symmetry.

To describe the larger-scale Z_2 symmetry breaking associated with the formation and coarsening of superclusters, we introduce an Ising variable σ_i at every lattice site such that $\sigma_i = +1$ (-1) if the f electron closest to site i belongs to the A (B) sublattice. Based on this definition, Fig. 3 *A–C*, *Bottom* shows the three Ising configurations $\{\sigma_i\}$ that correspond to the respective f-electron distribution $\{n_i^f\}$ shown in Fig. 3 *A–C*, *Top*. In terms of the Ising spin language, the clustering of checkerboards into superclusters thus corresponds to the growth of Ising ferromagnetic domains.

It is worth noting that there are two simultaneous phase-ordering processes during the temperature quench: the conventional CDW-metal phase separation at smaller scales (Fig. 2) and the coarsening of superclusters or effective Ising domains at larger scales (Fig. 3). Importantly, the conventional picture of phase-separated states with CDW order does not necessarily imply the emergence of superclusters observed here. As the f electrons in a CDW cluster can reside on either A or B sublattice, a CDW cluster can be characterized by a Z_2 variable $P = \pm 1$, which is called polarity for convenience. Naively, one expects the coexistence of CDW clusters of opposite polarities in a phase-separated state. Our simulation results thus indicate that the energy of the mixed-phase states can be further reduced through the "alignment" of CDW clusters, namely the formation of superclusters consisting of CDWs of the same polarity. As is discussed below, this alignment results from a nonlocal interaction mediated by the c electrons.

To characterize the growth of Ising domains associated with the superclusters, we compute the structure factor of the Ising spins: $S(\mathbf{k}, t) = \left| \frac{1}{N} \sum_i \sigma_i(t) \exp(i\mathbf{k} \cdot \mathbf{r}_i) \right|^2$. The ferromagnetic ordering implies that $S(\mathbf{k}, t)$ exhibits a growing peak at $\mathbf{k} = 0$. The inverse of the width of this peak can be used as a measure of the characteristic length scale of the superclusters: $L^{-1}(t) \sim \Delta k = \sum_{\mathbf{k}} S(\mathbf{k}, t)|\mathbf{k}| / \sum_{\mathbf{k}} S(\mathbf{k}, t)$. Using this characteristic length as a scale factor, Fig. 3*D* shows the scaled time-dependent structure factor versus the dimensionless momentum $|\mathbf{k}|L(t)$. As can be seen from Fig. 3*D*, the data points at different times collapse roughly on the same curve, indicating that the coarsening of the Ising domains exhibits a dynamical scaling; i.e., $S(\mathbf{k}, t) = L^2(t)\mathcal{G}[|\mathbf{k}|L(t)]$, where $\mathcal{G}(x)$ is a universal scaling function. The $1/k^3$ power-law tail at large momenta, consistent with the two-dimensional (2D) Porod's law (20), results from the sharp interfaces between the two different types of Ising domains or superclusters with opposite polarities.

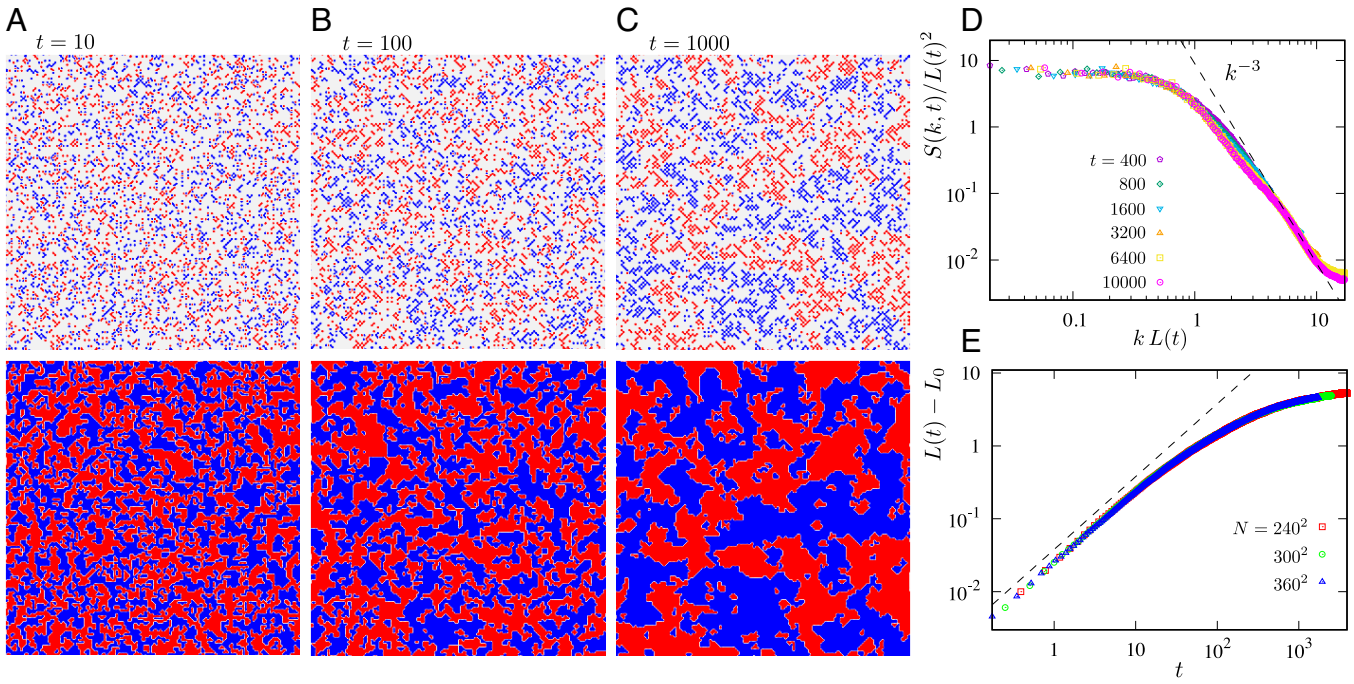

Fig. 3. Summary of the same ML-kMC simulations shown in Fig. 2 with emphasis on the coarsening of superclusters due to a hidden broken sublattice symmetry. (*A–C*) Snapshots of the *f*-electron configuration $\{n_i^f\}$ with blue and red dots indicating *f* electrons on the A and the B sublattice, respectively. The white regions (free of red/blue squares) are the same as those in Fig. 2 *A–C*; both represent the metallic phase. The corresponding Ising configurations $\{\sigma_i\}$ that characterize the Z_2 symmetry-breaking domains associated with superclusters are shown in *A–C*, *Bottom*. (*D*) Scaling plot of the time-dependent structure factor $S(\mathbf{k}, t)$ obtained from Fourier transform of the Z_2 order parameter. The dashed line shows the k^{-3} Porod's law in 2D. (*E*) Characteristic length $L(t)$ of the superclusters as a function of time for three different lattice sizes. The dashed line indicates the linear growth $L(t) - L_0 = \Delta L(t) \sim t$. The bending of the $L(t)$ curves at late times in this log-log plot indicates a logarithmic-like growth that is slower than the power law.

The order parameter ϕ describing this Z_2 symmetry breaking is then given by the magnetization density of Ising spins; i.e., $\phi = \langle \sigma_i \rangle$. It is worth noting that ϕ is not conserved in the kMC dynamics of the f electron. Phenomenologically, such a nonconserved field is governed by the time-dependent Ginzburg–Landau equation (TDGL) or model-A dynamics (24). The resultant domain coarsening is characterized by the $L \sim t^{1/2}$ Allen–Cahn power law (18, 19). However, as we show next, the coarsening of superclusters in our case does not follow the expected power law due to an unusual self-confinement of the f electrons.

The characteristic length $L(t)$ extracted from the structure factor is shown in Fig. 3*E* as a function of time for three different lattice sizes. Interestingly, except for a short initial period (up to $t \sim 10$), the growth of this length scale does not follow the expected power law, especially at late times. Moreover, even the initial seemingly power-law growth is not consistent with the $\alpha = 1/2$ Allen–Cahn law. Instead, L seems to increase linearly with time in this initial regime. To understand this anomalous behavior, we note that the TDGL equation or the Allen–Cahn theory describes an interface-controlled domain growth where the interfacial velocity is proportional to the curvature of the domain interface (58). On the other hand, since the Z_2 order parameter in our case is defined by whether the aggregating f electrons are on the A or B sublattice, the resultant domain growth needs not rely on the expansion of an existing boundary. Instead, a supercluster can quickly increase its size as f electrons in its neighborhood move from one sublattice to another via only a nearest-neighbor hopping. Due to such collective movement of f electrons, the growth of the superclusters exhibits an avalanche-like behavior similar to the Barkhausen effect in magnetic domain growth. A faster linear growth of the superclusters thus arises from such avalanche dynamics at the early stage. As is discussed below, such collective behavior is induced by an effective nonlocal interaction between f electrons.

Although the repulsion U between the two types of electrons is local in the FK model, the heavier f electrons experience an effective long-range interaction mediated by the itinerant c electrons. In particular, due to this nonlocal interaction, the presence of a checkerboard cluster creates a staggered potential in its neighborhood that takes alternating values on neighboring sites of the bipartite lattice. This effective potential is illustrated in Fig. 4*A* where a test f electron is placed in the neighborhood of a checkerboard cluster at the center. Exact MC simulation was used to obtain the frequency ν_i that the test particle stays at site i, from which the potential is computed: $V_i = -k_B\,T \log \nu_i$. As shown in Fig. 4*A*, the effective potential field $V(\mathbf{r}_i)$ exhibits the same staggered pattern whose polarity is determined by that of the center checkerboard cluster. Consequently, f electrons in the neighborhood of this checkerboard cluster tend to be trapped in the same sublattice. Also importantly, this staggered potential causes existing checkerboards in the neighborhood to change its polarity, thus leading to the formation of a supercluster and its subsequent growth that is not captured by the interface-controlled mechanism.

At a late stage of the phase separation, a much slower logarithmic-like growth sets in for superclusters, as shown in Fig. 3*E*. Interestingly, exactly the same staggered potential discussed above is also responsible for the stalled growth of the Ising domains and, in fact, of the smaller checkerboard clusters as well. To understand this unusual freezing behavior, we note that while the strength of the staggered potential increases with the size of CDW cluster from which it originates, the energy barrier ΔV_{AB} between the two sublattices is also enhanced as more and more checkerboards merge to form a larger supercluster. To demonstrate this effect, we consider different geometrical arrangements of

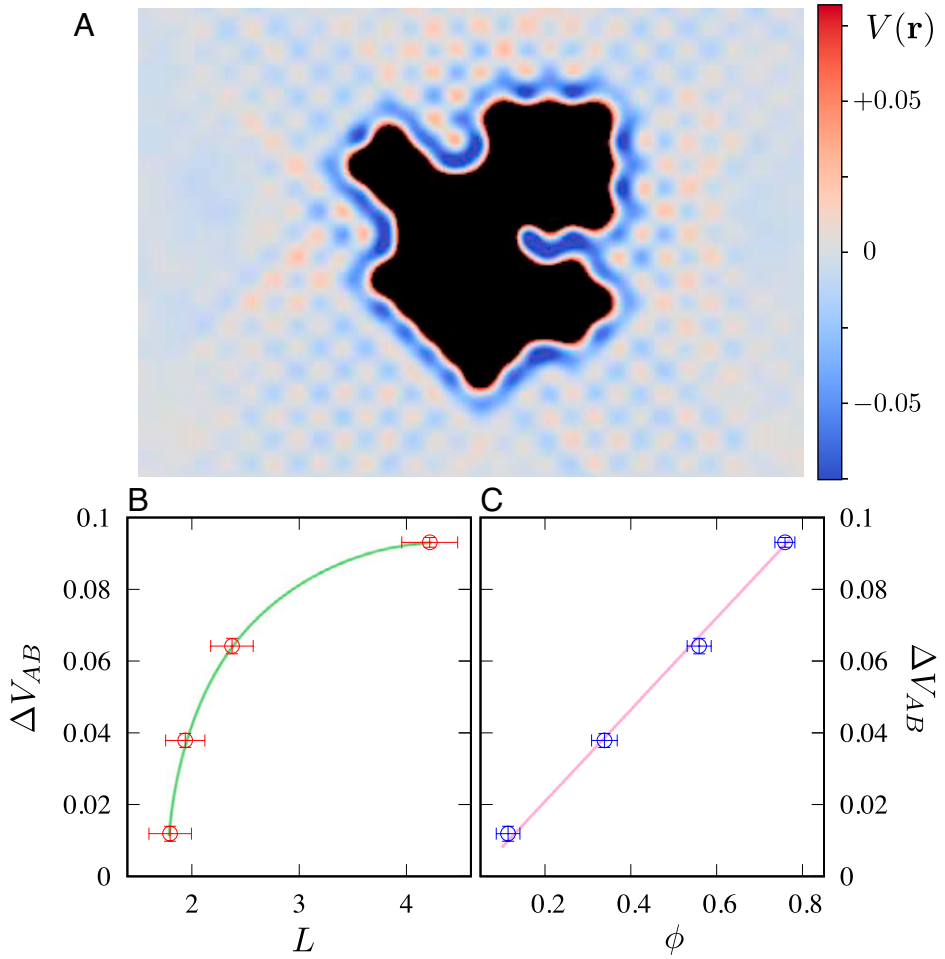

Fig. 4. (*A*) Density plot of effective potential $V(\mathbf{r}_i) = -k_B T \log \nu_i$ for f electrons created by a checkerboard cluster at the center. The potential field $V(\mathbf{r})$ exhibits the same staggering patten as that of the checkerboard cluster at the center. f electrons in the neighborhood thus tend to reside on the same sublattice, leading to the growth of the supercluster. (*B* and *C*) The depth of the staggering potential, given by the averaged potential difference between the two sublattices ΔV_{AB} versus (*B*) the characteristic length L of superclusters and (*C*) the Ising order parameter ϕ.

a finite number of checkerboard clusters on a 30×30 lattice, giving rise to different shapes and sizes of superclusters or Ising domains. MC simulation with exact diagonalization is then used to compute the resultant effect potential $V(\mathbf{r}_i)$ for the f electrons; details can be found in *SI Appendix*, section S3. The average potential difference between the A/B sublattices $\Delta V_{AB} = \langle \frac{1}{N/2} \left| \sum_{i \in \mathrm{A}} V_i - \sum_{i \in \mathrm{B}} V_i \right| \rangle$ is shown in Fig. 4*B* as a function of the numerically obtained characteristic length L of the Ising domains. The staggered potential ΔV_{AB} indeed increases with the size of the superclusters. Moreover, we observe an intriguing linear dependence of the potential barrier ΔV_{AB} on the effective Ising order parameter ϕ, as shown in Fig. 4*C*.

Importantly, the fact that the energy barrier ΔV_{AB} increases with the size of the Ising domains also explains the freezing behaviors observed in our ML-kMC simulations. As the size L of superclusters increases with time, the potential difference between the two sublattices becomes so strong that individual f electrons are deeply trapped at one sublattice and cannot hop to the neighboring sites. For example, consider a checkerboard cluster on sublattice A in Fig. 4*A* and a test particle sitting at a site that belongs to the lower-energy sublattice A. Although the checkerboard at the center has a strong affinity to the new particle, as evidenced by the rather low potential energy at the edge of the cluster, the large energy barrier at the B sublattice prevents the f electron from joining the cluster. The reduced mobility of the f electron thus results in an arrested coarsening of both the superclusters and the smaller-sized checkerboard clusters.

To summarize, by utilizing modern machine-learning techniques, we have successfully developed a neural network energy model that allows us to perform a large-scale kinetic Monte Carlo simulation on the well-studied FK model. We discover an unusual phase-ordering phenomenon where domain coarsening occurs simultaneously at two different scales: the growth of checkerboard clusters and the expansion of Ising domains associated with a hidden broken sublattice symmetry. The competition of these two processes leads to an anomalously slow phase separation. Several interesting dynamical phenomena, such as the early-stage avalanche domain growth and the decelerated coarsening of superclusters, require further investigation and will be left for future work.

Unusual domain coarsening has been reported in classical systems, which is often related to frustrated interactions or quenched disorder (59–63). In this work we describe a freezing mechanism that arises from the interaction of itinerant c electrons and classical f electrons. Similar glassy dynamics could be generic for phase ordering in other correlated electron systems. A characteristic feature of correlated electron materials is the coexistence of fast electron quasiparticles and slow bosonic or collective degrees of freedom. The nontrivial interplay between these two sets of variables could lead to dynamical phenomena that are unique to

correlated electrons. Given the complexity of such systems, we envision ML techniques as an indispensable tool for multiscale modeling of nonequilibrium dynamics driven by the electron correlation effect.

Data Availability. The relevant C and Python codes, the trained neural-network model, and sample training datasets can be found in the GitHub repository, https://github.com/cherngroupUVA/Falicov_Kimball_ML_data. All study data are included in this article and/or *SI Appendix*.

ACKNOWLEDGMENTS. This work was supported by the US Department of Energy Basic Energy Sciences under Contract DE-SC0020330. We acknowledge Research Computing at The University of Virginia for providing computational resources and technical support that have contributed to the results reported within this publication.

1. M. Uehara, S. Mori, C. H. Chen, S.-W. Cheong, Percolative phase separation underlies colossal magnetoresistance in mixed-valent manganites. *Nature* **399**, 560–563 (1999).
2. T. Miao *et al.*, Direct experimental evidence of physical origin of electronic phase separation in manganites. *Proc. Natl. Acad. Sci. U.S.A.* **117**, 7090–7094 (2020).
3. T. Hanaguri *et al.*, A 'checkerboard' electronic crystal state in lightly hole-doped $Ca_{2-x}Na_xCuO_2Cl_2$. *Nature* **430**, 1001–1005 (2004).
4. M. H. Hamidian *et al.*, Detection of a cooper pair density wave in $Bi_2Sr_2CaCu_2O_{8+x}$. *Nature* **532**, 343–347 (2016).
5. V. J. Emery, S. A. Kivelson, J. M. Tranquada, Stripe phases in high-temperature superconductors. *Proc. Natl. Acad. Sci. U.S.A.* **96**, 8814–8817 (1999).
6. E. Dagotto, *Nanoscale Phase Separation and Colossal Magnetoresistance* (Springer, Berlin, Germany, 2002).
7. E. Dagotto, Complexity in strongly correlated electronic systems. *Science* **309**, 257–262 (2005).
8. S. A. Kivelson, E. Fradkin, V. J. Emery, Electronic liquid-crystal phases of a doped Mott insulator. *Nature* **393**, 550–553 (1998).
9. E. Fradkin, S. A. Kivelson, J. M. Tranquada, Theory of intertwined orders in high temperature superconductors. *Rev. Mod. Phys.* **87**, 457–482 (2015).
10. P. B. Visscher, Phase separation instability in the Hubbard model. *Phys. Rev. B* **10**, 943–945 (1974).
11. J. Zaanen, O. Gunnarsson, Charged magnetic domain lines and the magnetism of high-T_c oxides. *Phys. Rev. B Condens. Matter* **40**, 7391–7394 (1989).
12. M. Kato, K. Machida, H. Nakanishi, M. Fujita, Soliton lattice modulation of incommensurate spin density wave in two dimensional Hubbard model -A mean field study-. *J. Phys. Soc. Jpn.* **59**, 1047–1058 (1990).
13. V. J. Emery, S. A. Kivelson, H. Q. Lin, Phase separation in the t-J model. *Phys. Rev. Lett.* **64**, 475–478 (1990).
14. S. White, D. Scalapino, Phase separation and stripe formation in the two-dimensional t-J model: A comparison of numerical results. *Phys. Rev. B Condens. Matter Mater. Phys.* **61**, 6320–6326 (2000).
15. C.-H. Yee, L. Balents, Phase separation in doped Mott insulators. *Phys. Rev. X* **5**, 021007 (2015).
16. J. D. Gunton, M. San Miguel, P. S. Saint, "The dynamics of first order phase transitions" in *Phase Transitions and Critical Phenomena*, C. Domb, J. L. Lebowitz, Eds. (Academic, New York, NY, 1983), vol. 8, pp. 269–466.
17. P. L. Krapivsky, S. Redner, E. Ben-Naim, *A Kinetic View of Statistical Physics* (Cambridge University Press, 2010).
18. A. J. Bray, Theory of phase-ordering kinetics. *Adv. Phys.* **43**, 357–459 (1994).
19. A. Onuki, *Phase Transition Dynamics* (Cambridge University Press, Cambridge, UK, 2002).
20. S. Puri, V. Wadhawan, Eds., *Kinetics of Phase Transitions* (CRC Press, Taylor & Francis Group, London, UK, 2009).
21. Y. Oono, S. Puri, Study of phase-separation dynamics by use of cell dynamical systems. I. Modeling. *Phys. Rev. A Gen. Phys.* **38**, 434–453 (1988).
22. J. D. Gunton, R. Toral, A. Chakrabarti, Numerical studies of phase separation in models of binary alloys and polymer blends. *Phys. Scr. T* **33**, 12–19 (1990).
23. R. Weinkamer, P. Fratzl, H. S. Gupta, O. Penrose, J. L. Lebowitz, Using kinetic Monte Carlo simulations to study phase separation in alloys. *Phase Transit.* **77**, 433–456 (2004).
24. P. C. Hohenberg, B. I. Halperin, Theory of dynamic critical phenomena. *Rev. Mod. Phys.* **49**, 435–479 (1977).
25. H. Furukawa, A dynamic scaling assumption for phase separation. *Adv. Phys.* **34**, 703–750 (1985).
26. L. M. Falicov, J. C. Kimball, Simple model for semiconductor-metal transitions: SmB_6 and transition-metal oxides. *Phys. Rev. Lett.* **22**, 997–999 (1969).
27. J. Hubbard, Electron correlations in narrow energy bands III. An improved solution. *Proc. R. Soc. Lond. A Math. Phys. Sci.* **281**, 401–419 (1964).
28. J. K. Freericks, V. Zlatić, Exact dynamical mean-field theory of the Falicov-Kimball model. *Rev. Mod. Phys.* **75**, 1333–1382 (2003).
29. T. Kennedy, E. H. Lieb, An itinerant electron model with crystalline or magnetic long range order. *Physica A* **138**, 320–358 (1986).
30. J. K. Freericks, E. H. Lieb, D. Ueltschi, Phase separation due to quantum mechanical correlations. *Phys. Rev. Lett.* **88**, 106401 (2002).
31. J. K. Freericks, R. Lemański, Segregation and charge-density-wave order in the spinless Falicov-Kimball model. *Phys. Rev. B Condens. Matter Mater. Phys.* **61**, 13438–13444 (2000).
32. G. I. Watson, R. Lemanski, The ground-state phase diagram of the two-dimensional Falicov-Kimball model. *J. Phys. Condens. Matter* **7**, 9521–9542 (1995).
33. R. Lemański, J. K. Freericks, G. Banach, Stripe phases in the two-dimensional Falicov-Kimball model. *Phys. Rev. Lett.* **89**, 196403 (2002).
34. R. Lemański, J. K. Freericks, G. Banach, Charge stripes due to electron correlations in the two-dimensional spinless Falicov-Kimball Model. *J. Stat. Phys.* **116**, 699–718 (2004).
35. M.-T. Tran, Inhomogeneous phases in the Falicov-Kimball model: Dynamical mean-field approximation. *Phys. Rev. B Condens. Matter Mater. Phys.* **73**, 205110 (2006).
36. M. M. Maśka, K. Czajka, Pattern formation in the Falicov-Kimball model. *Phys. Status Solidi* **242**, 479–483 (2005).
37. M. M. Maśka, K. Czajka, Thermodynamics of the two-dimensional Falicov-Kimball model: A classical Monte Carlo study. *Phys. Rev. B Condens. Matter Mater. Phys.* **74**, 035109 (2006).
38. A. E. Antipov, Y. Javanmard, P. Ribeiro, S. Kirchner, Interaction-tuned Anderson versus Mott localization. *Phys. Rev. Lett.* **117**, 146601 (2016).
39. G. T. Barkema, "Monte Carlo simulations of domain growth" in *Kinetics of Phase Transitions*, S. Puri, V. Wadhawan, Eds. (CRC Press, Taylor & Francis Group, London, UK, 2009), chap. 3, pp. 101–120.
40. D. Marx, J. Hutter, *Ab Initio Molecular Dynamics: Basic Theory and Advanced Methods* (Cambridge University Press, Cambridge, UK, 2009).
41. P. Fratzl, R. Weinkamer, "Phase separation in binary alloys – Modelling approaches" in *Moving Interfaces in Crystalline Solids*, F. D. Fischer, Ed. (Springer, New York, NY, 2004), pp. 57–116.
42. A. B. Bortz, M. H. Kalos, J. L. Lebowitz, M. A. Zendejas, Time evolution of a quenched binary alloy: Computer simulation of a two-dimensional model system. *Phys. Rev. B* **10**, 535–541 (1974).
43. A. Weisse, G. Wellein, A. Alvermann, H. Fehske, The kernel polynomial method. *Rev. Mod. Phys.* **78**, 275–306 (2006).
44. J. Behler, M. Parrinello, Generalized neural-network representation of high-dimensional potential-energy surfaces. *Phys. Rev. Lett.* **98**, 146401 (2007).
45. A. P. Bartók, M. C. Payne, R. Kondor, G. Csányi, Gaussian approximation potentials: The accuracy of quantum mechanics, without the electrons. *Phys. Rev. Lett.* **104**, 136403 (2010).
46. L. Zhang, J. Han, H. Wang, R. Car, W. E, Deep potential molecular dynamics: A scalable model with the accuracy of quantum mechanics. *Phys. Rev. Lett.* **120**, 143001 (2018).
47. H. Suwa *et al.*, Machine learning for molecular dynamics with strongly correlated electrons. *Phys. Rev. B* **99**, 161107 (2019).
48. F. Noé, A. Tkatchenko, K.-R. Müller, C. Clementi, Machine learning for molecular simulation. *Annu. Rev. Phys. Chem.* **71**, 361–390 (2020).
49. P. Zhang, P. Saha, G.-W. Chern, Machine learning dynamics of phase separation in correlated electron magnets. arXiv [Preprint] (2020). https://doi.org/10.48550/arXiv.2006.04205 (Accessed 7 June 2020).
50. P. Zhang, G.-W. Chern, Arrested phase separation in double-exchange models: Large-scale simulation enabled by machine learning. *Phys. Rev. Lett.* **127**, 146401 (2021).
51. W. Kohn, Density functional and density matrix method scaling linearly with the number of atoms. *Phys. Rev. Lett.* **76**, 3168–3171 (1996).
52. E. Prodan, W. Kohn, Nearsightedness of electronic matter. *Proc. Natl. Acad. Sci. U.S.A.* **102**, 11635–11638 (2005).
53. J. Ma, P. Zhang, Y. Tan, A. W. Ghosh, G.-W. Chern, Machine learning electron correlation in a disordered medium. *Phys. Rev. B* **99**, 085118 (2019).
54. I. M. Lifshitz, V. V. Slyozov, The kinetics of precipitation from supersaturated solid solutions. *J. Phys. Chem. Solids* **19**, 35–50 (1961).
55. C. Wagner, Theorie der Alterung von Niederschlagen durch Umlosen. *Z. Elektrochem* **65**, 581–591 (1961).
56. J. W. Cahn, J. E. Hilliard, Free energy of a nonuniform system. I. Interfacial free energy. *J. Chem. Phys.* **28**, 258–267 (1958).
57. D. A. Huse, Corrections to late-stage behavior in spinodal decomposition: Lifshitz-Slyozov scaling and Monte Carlo simulations. *Phys. Rev. B Condens. Matter* **34**, 7845–7850 (1986).
58. S. M. Allen, J. W. Cahn, A microscopic theory for antiphase boundary motion and its application to antiphase domain coarsening. *Acta Metall.* **27**, 1085–1095 (1979).
59. J. D. Shore, M. Holzer, J. P. Sethna, Logarithmically slow domain growth in nonrandomly frustrated systems: Ising models with competing interactions. *Phys. Rev. B Condens. Matter* **46**, 11376–11404 (1992).
60. M. R. Evans, Anomalous coarsening and glassy dynamics. *J. Phys. Condens. Matter* **14**, 1397–1422 (2002).
61. H. Tanaka, Viscoelastic phase separation. *J. Phys. Condens. Matter* **12**, R207–R264 (2000).
62. M. Zannetti, "Aging in domain growth" in *Kinetics of Phase Transitions*, S. Puri, V. Wadhawan, Eds. (CRC Press, Boca Raton, FL, 2009), pp. 153–202.
63. F. Corberi, Coarsening in inhomogeneous systems. *C. R. Phys.* **16**, 332–342 (2015).